Dalton Transactions

ROYAL SOCIETY OF CHEMISTRY

PAPER

View Article Online
View Journal | View Issue

Cite this: *Dalton Trans.*, 2025, **54**, 8430

Controlled synthesis of hierarchical hollow $Co_xNi_{3-x}S_4$ towards enhanced rate capability and excellent cycling stability†

Xiankun Xiong,[a,b] Chaochao Lu,[b] Zhongliang Pi,[b] CunYuan Pei*[a] and Cheng Du *[b]

The strategic design and advancement of electrode materials are crucial for the effectiveness of energy storage and conversion devices. Herein, we successfully synthesized a series of $Co_xNi_{3-x}S_4$ hollow microspheres through a combined hydrothermal and vapor-phase sulfidation process. These microspheres are composed of interlinked nanosheets featuring uniformly distributed nanoparticles on their surfaces. This distinctive hierarchical structure integrates one-dimensional, two-dimensional and three-dimensional elements, thereby facilitating the exposure of more active sites, enhancing electrolyte–active site interactions, accelerating carrier transport, and mitigating volume expansion during cycling. Specifically, varying the molar ratios results in different nanosheet thicknesses, with higher cobalt content leading to thicker nanosheets and higher nickel content producing thinner ones. The optimized $(Co_1Ni_2)S_4$ electrode material exhibits an impressive specific capacity of 204.9 mA h g^{-1} (1639 F g^{-1}) at 1 A g^{-1}, along with remarkable rate capability (holding 80.5% when the current is increased 20 times) and exceptional cycling stability (maintaining 96% of its initial capacity after 15 000 cycles). When paired with lotus pollen-derived activated carbon (AC) to form a supercapacitor device, the $(Co_1Ni_2)S_4$//AC configuration reaches an energy density of 66.5 W h kg^{-1} at 800 W kg^{-1}. Notably, even after 30 000 cycles, the device retains an outstanding 98% of its initial capacity while sustaining 100% coulombic efficiency. This study presents an encouraging method for the precise fabrication of advanced bimetallic sulfides with enhanced electrochemical characteristics, facilitating their broader application in energy storage technologies.

Received 10th February 2025,
Accepted 21st April 2025

DOI: 10.1039/d5dt00317b

rsc.li/dalton

1. Introduction

As non-renewable energy sources are progressively depleted and environmental issues stemming from fossil fuel combustion become more pronounced, there is an urgent need to cultivate renewable energy alternatives to tackle energy scarcity and mitigate global warming.[1–3] Consequently, advancing cutting-edge technologies for energy storage and conversion has become indispensable.[4–7] Supercapacitors (SCs) have garnered significant attention owing to their exceptional power density, rapid charging capabilities, outstanding cycling durability, and environmental compatibility.[8,9] Within SCs, the choice of electrode materials significantly influences the electrochemical performances of these devices.[10–12] To date, various metallic compounds like hydroxides and oxides have been thoroughly studied and employed in supercapacitor technology.[13–15] Nonetheless, these materials' subpar electrochemical properties and limited electrical conductivity have impeded their extensive commercial adoption in electrode systems.[16,17] Hence, the development of superior electrode materials is pivotal to achieving optimal energy storage and power delivery in supercapacitors.

Transition metal sulfides (TMSs) are gaining attention as potentially valuable pseudocapacitive materials for supercapacitor applications due to their advantages of low cost, rich resources, high theoretical specific capacitance, favorable conductivity, and rapid redox kinetics. Various TMSs, including NiS, CoS, Co_3S_4, FeS and MnS, have been investigated as potential electrode materials for SCs.[18–22] These materials offer a compelling combination of properties that can significantly enhance the performance and economic viability of SCs, making them an attractive focus for ongoing research and development in energy storage technologies.[23–26] Despite their advantages, simple TMSs exhibit insufficient cycling stability

[a]*College of Materials & Chemical Engineering, China Three Gorges University, Yichang, 443002, China. E-mail: 1154917949@qq.com*
[b]*Hubei Key Lab for Processing and Application of Catalytic Materials, College of Chemistry and Chemical Engineering, Huanggang Normal University, Huanggang, 437000, China. E-mail: ducheng20141020@163.com*
† Electronic supplementary information (ESI) available. See DOI: https://doi.org/10.1039/d5dt00317b

and rate performance, largely due to significant volume changes during repeated charge–discharge cycles. Introducing multiple metallic elements into the material can shift the Fermi level, improving interfacial electron transfer and markedly enhancing electrochemical activity.[27] Generally, cobalt compounds are noted for their excellent cycling stability, though with comparatively lower capacitance. In contrast, nickel compounds provide higher capacitance but exhibit less stable cycling performance.[28] By combining cobalt and nickel into Co–Ni-based composites, it is possible to leverage the high capacitance of nickel compounds alongside the superior cycling stability of cobalt compounds.[29–31] This integration significantly boosts the overall electrochemical performance of the electrode materials.

In addition, hollow-structured electrode materials have addressed the limitations of traditional electrodes by providing a high surface area, shortened ion/electron diffusion paths, and enhanced anti-agglomeration properties. These features improve ion transport efficiency and structural integrity, leading to better performance in electrochemical devices. For instance, Liu's team synthesized hollow rod-like NiCoMn ternary metal sulfides from metal–organic frameworks. When paired with activated carbon in an ASC, this material achieved an energy density of 50 W h kg^{-1} at 850 W kg^{-1}.[32] Qi *et al.* synthesized CoNiS hollow nanocages derived from ZIF-67, which exhibited remarkable electrochemical performance. These hollow nanocages demonstrated a high capacity of 598.8 C g^{-1} at 1 A g^{-1} and maintained impressive cycling stability, retaining 70.1% of their capacity after 10 000 cycles.[33] While employing metal–organic frameworks (MOFs) as templates for the synthesis of hollow structures provides benefits like precise morphological control and high specific surface area, it has several drawbacks too. The synthesis process can be complex and requires stringent conditions, leading to higher costs. Additionally, there is a risk of residual organic ligands that may affect the final material's performance. These challenges pose significant limitations to its large-scale application.

Herein, we fabricate hollow $Co_xNi_{3-x}S_4$ microspheres *via* a convenient solvothermal method followed by gas-phase sulfidation. Importantly, the molar ratio of cobalt and nickel salts significantly influences both the structural morphology and the electrochemical properties of the resulting $Co_xNi_{3-x}S_4$. Among the synthesized materials, the $(Co_1Ni_2)S_4$ hollow spheres stand out as they are composed of interwoven thin nanosheets, with nanoparticles grown on the surfaces of these nanosheets. This unique nanoarchitecture not only provides a three-dimensional framework that can effectively accommodate volume changes during cycling, but also boosts the surface area and unveils more active sites, contributing to an outstanding specific capacity, superior rate performance, and exceptional cycling durability. When integrated with activated carbon to form an asymmetric supercapacitor (ASC), $(Co_1Ni_2)S_4$//AC demonstrates high energy and power densities, making it a promising candidate for advanced energy storage applications.

2. Experimental details

2.1. Synthesis of CoNi-precursors

Dissolve different molar ratios (1 : 1, 1 : 2, and 1 : 4) of $Co(NO_3)_2{\cdot}6H_2O$ and $Ni(NO_3)_2{\cdot}6H_2O$ in 60 mL of isopropanol, ensuring that the total molar concentration remains at 1 mmol. Stir the mixture until a uniform pink solution forms. Introduce 12 mL of glycerol into the solution while continuously stirring. Transfer this combined mixture to an autoclave and heat it at 160 °C for 6 hours. Following the reaction, separate the resulting precipitate by centrifugation and clean it with water and ethanol. Dry the precipitate under vacuum at 60 °C for 12 hours.

Suspend the dried powder obtained from the previous step in 60 mL of deionized water and return it to the 100 mL autoclave. Perform hydrothermal treatment at 150 °C for 5 hours. After the reaction, isolate the precipitate through centrifugation and wash it with deionized water. Vacuum-dry the sample at 60 °C for an additional 12 hours.

2.2. Synthesis of $Co_xNi_{3-x}S_4$ spheres

Place the CoNi-precursors into a tube furnace and perform sulfidation using thiourea as the sulfur source. Heat the furnace to 220 °C at a ramping rate of 2 °C min^{-1} under Ar and maintain this temperature for 2 hours.

3. Results and discussion

The fabrication process of $Co_xNi_{3-x}S_4$ hierarchical hollow microspheres, featuring ultrathin nanosheets with nanoparticles on their surfaces, is schematically illustrated in Fig. 1. The method comprises two steps: the hydrothermal synthesis of CoNi-precursors and their subsequent sulfidation using thiourea. As observed in Fig. S1,† the Co_1Ni_2-precusors are composed of smooth, thin-layered nanosheets that form hollow microspheres with diameters of about 1 μm. The hollow interior likely arises due to the Kirkendall effect.[34,35] Additionally, X-ray Diffraction (XRD) analysis confirms that the Co_1Ni_2-precusors consist of cobalt–nickel hydroxide (Fig. S2†). As revealed by scanning electron microscopy (SEM), the morphology of $(Co_1Ni_2)S_4$ remains largely intact after sulfidation, though the surfaces of the nanosheets become noticeably rougher (Fig. 2a–c). To further examine the structure of $(Co_1Ni_2)S_4$, we conducted transmission electron microscopy (TEM) analysis. The TEM images confirm that these sulfides form hollow microspheres assembled from interwoven and

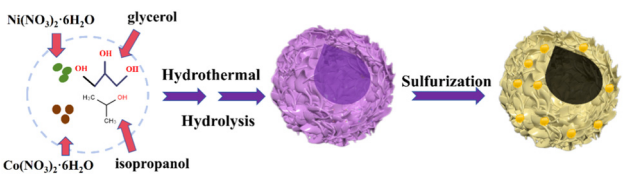

Fig. 1 The schematic representation of the formation of $Co_xNi_{3-x}S_4$.

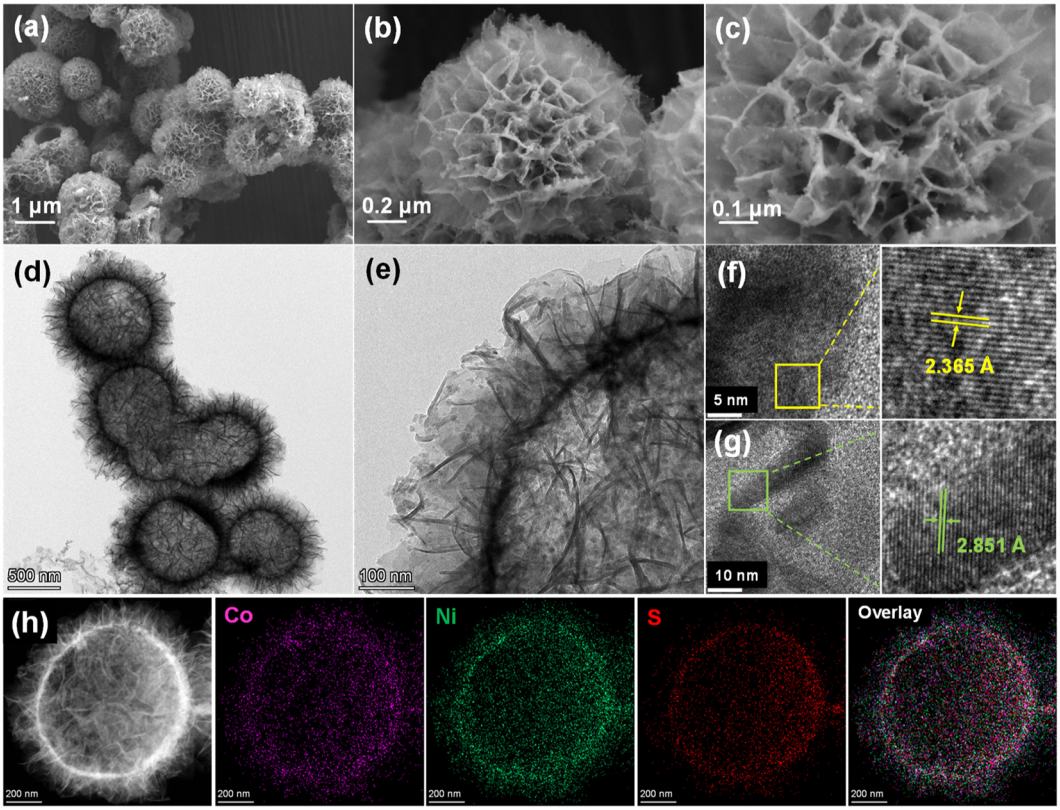

Fig. 2 (a–c) SEM and (d–g) TEM images of $(Co_1Ni_2)S_4$ and (h) elemental mapping of Co, Ni, and S elements of $(Co_1Ni_2)S_4$.

curled nanosheets, consistent with the SEM findings (Fig. 2d). High-resolution microscopy (Fig. 2e) additionally shows uniformly distributed nanoparticles on the nanosheet surfaces. This hierarchical architecture, which combines one-dimensional, two-dimensional, and three-dimensional elements, greatly increases the active surface area, enhances the interaction between the electrolyte and active sites, speeds up electron/ion transport, and reduces volume expansion during cycling. As illustrated in Fig. 3f and g, the lattice fringe spacing of 2.365 Å falls between the (004) plane of Ni_3S_4 (PDF# 43-1469) and the (400) plane of Co_3S_4 (PDF# 42-1448), while the spacing of 2.851 Å is situated between the (113) plane of Ni_3S_4 and the (311) plane of Co_3S_4. Furthermore, EDS mapping (Fig. 3h) indicates that the distribution of Co, Ni, and S elements is uniform across the hollow microsphere structure. These structural characteristics demonstrate the successful production of cobalt–nickel bimetallic sulfides. Interestingly, our findings indicate that the presence of cobalt and nickel salts, along with their molar ratios, significantly influences the structure of the hollow microspheres. As shown in Fig. S4,† in the absence of either cobalt or nickel salts, the microspheres primarily consist of large nanoparticles. Increasing the molar ratio of cobalt salt results in thicker nanosheets forming hollow spheres, whereas a higher molar ratio of nickel salt leads to thinner nanosheets (Fig. S5†). To conduct a detailed elemental analysis, ICP-OES was employed. The findings, presented in Table S1,† reveal a significant correspondence between the molar ratio of Co to Ni as determined by experiments and the original feed ratio.

The phase structure of the $Co_xNi_{3-x}S_4$ materials was examined using XRD analysis. As depicted in Fig. S6,† the characteristic diffraction peaks at 31.6°, 35.3°, 38.8°, 45.3°, 53.6°and 61.2° correspond to the (200), (210), (211), (220), (311) and (321) planes of NiS_2 (PDF# 11-0099), respectively. Meanwhile, the peaks at 31.3°, 37.9°, 50.0° and 54.7° match the (311), (400), (511) and (440) planes of Ni_3S_4 (PDF# 47-1739), respectively. These results indicate that the nickel sulfide is composed of a mixed-phase structure. The main peaks at 30.5°, 35.3°, 47.0° and 54.3° can be identified as those of CoS (PDF# 75-0605). As illustrated in Fig. 3a, the XRD peaks of cobalt–nickel bimetallic sulfides are situated between the standard peaks of Co_3S_4 (PDF# 42-1448) and Ni_3S_4 (PDF# 43-1469). When the nickel ratio increases, the diffraction peaks shift closer to those of Ni_3S_4, whereas an increase in the cobalt ratio brings the lattice constants closer to the standard values of Co_3S_4. This indicates that adjusting the ratios of cobalt and nickel can effectively control the lattice parameters and physicochemical properties of the material. N_2 adsorption–desorption isotherms were utilized to assess the specific surface area and pore size distribution of $(Co_1Ni_2)S_4$. As displayed in Fig. S8a,† the isotherm displays a type IV curve, indicative of a well-defined mesoporous structure.[36,37] With a BET specific surface

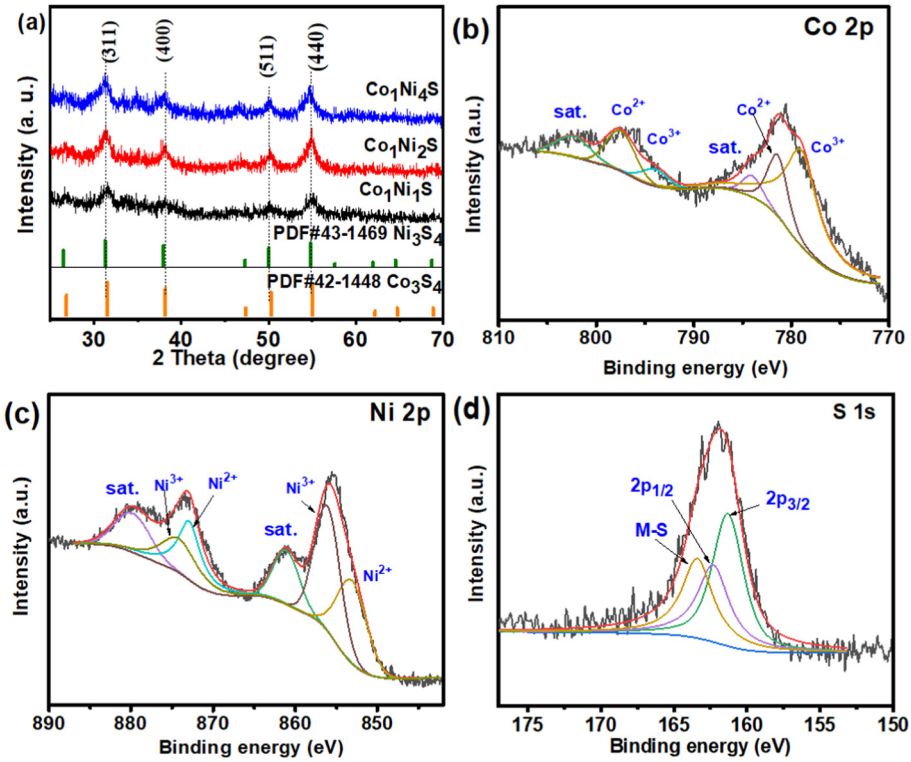

Fig. 3 (a) XRD for $Co_xNi_{3-x}S_4$ and XPS spectra of (b) the Co 2p, (c) Ni 2p, and (d) S 1s for $(Co_1Ni_2)S_4$.

area of 67.0 m^2 g^{-1}, the $(Co_1Ni_2)S_4$ material's pore size distribution analysis indicates that most pores are in the range of 10 to 20 nm.

By employing X-ray photoelectron spectroscopy (XPS), the electronic states of the elements within $(Co_1Ni_2)S_4$ were explored to provide a deeper look into its structure and composition, as indicated in Fig. S9† and Fig. 3b–e. The presence of Co, Ni, and S is confirmed by the XPS survey scan in Fig. S9,† aligning with the observations from elemental mapping. Fig. 3b displays two clear spin–orbit doublets that correspond to Co^{2+} and Co^{3+}.[38] In the Ni region (Fig. 3c), XPS reveals four main peaks: two peaks at 853.2 eV and 873.0 eV are linked to Ni^{2+}, while two peaks at 856.3 eV and 874.3 eV are indicative of Ni^{3+}.[39,40] The presence of these mixed oxidation states for both cobalt and nickel provides multiple redox couples, which can significantly enhance the material's electrochemical performance. Three principal peaks are observed in the S 2p spectrum (Fig. 3d) at binding energies of 163.3 eV, 162.3 eV, and 161.3 eV. With respect to metal–sulfur bonds, S $2p_{1/2}$ and S $2p_{3/2}$, these peaks indicate the inclusion of S^{2-} and strong metal–sulfur interactions in the material.[41]

Using a three-electrode electrochemical cell, the electrochemical properties of $Co_xNi_{3-x}S_4$ were thoroughly investigated *via* cyclic voltammetry (CV) and galvanostatic charge–discharge (GCD) tests. As illustrated in Fig. 4a, each CV curve exhibits a pair of distinct redox peaks, indicative of faradaic redox processes primarily associated with the valence changes of Ni^{2+}/Ni^{3+} and Co^{2+}/Co^{3+}/Co^{4+}.[42] Notably, the $(Co_1Ni_2)S_4$ electrode shows the largest integrated CV area, suggesting superior electrochemical storage capacity. Fig. 4b presents the CV curves of $(Co_1Ni_2)S_4$ at various scan rates ranging from 5 to 60 mV s^{-1}. The similarity in shapes across these curves highlights excellent rate capability, while minimal peak shifts at different scan rates indicate good reversibility.

To further investigate the relationship between the peak current density (i_p) and the scan rate (v) for $(Co_1Ni_2)S_4$ the equation $i_p = av^b$, where a and b are constants that can be adjusted to fit experimental data, is used. The exponent b plays a key role in identifying the nature of the charge storage mechanisms. When b is close to 0.5, it signifies that the charge storage mechanism is mainly driven by diffusion. A b value closer to 1.0 suggests that the charge storage process is predominantly governed by surface capacity. The fitted b values for the oxidation and reduction peaks of the $(Co_1Ni_2)S_4$ electrode, as shown in Fig. 4c, are 0.61 and 0.69. These values, within the range of $0.5 < b < 1$, suggest a combined mechanism involving both diffusion-controlled and surface capacity-controlled processes.

In addition, the capacitive contribution at various scan rates was assessed utilizing the equation $i = k_1v + k_2v^{1/2}$, where k_1v indicates the portion attributed to surface capacitance, whereas $k_2v^{1/2}$ reflects the impact of diffusion-limited processes.[43] As depicted in Fig. 4d, at a scan rate of 5 mV s^{-1}, the surface capacity contributes 25% to the overall charge storage, represented by the yellow-shaded portion within the CV curve. With an increase in the scan rate, the proportion of surface

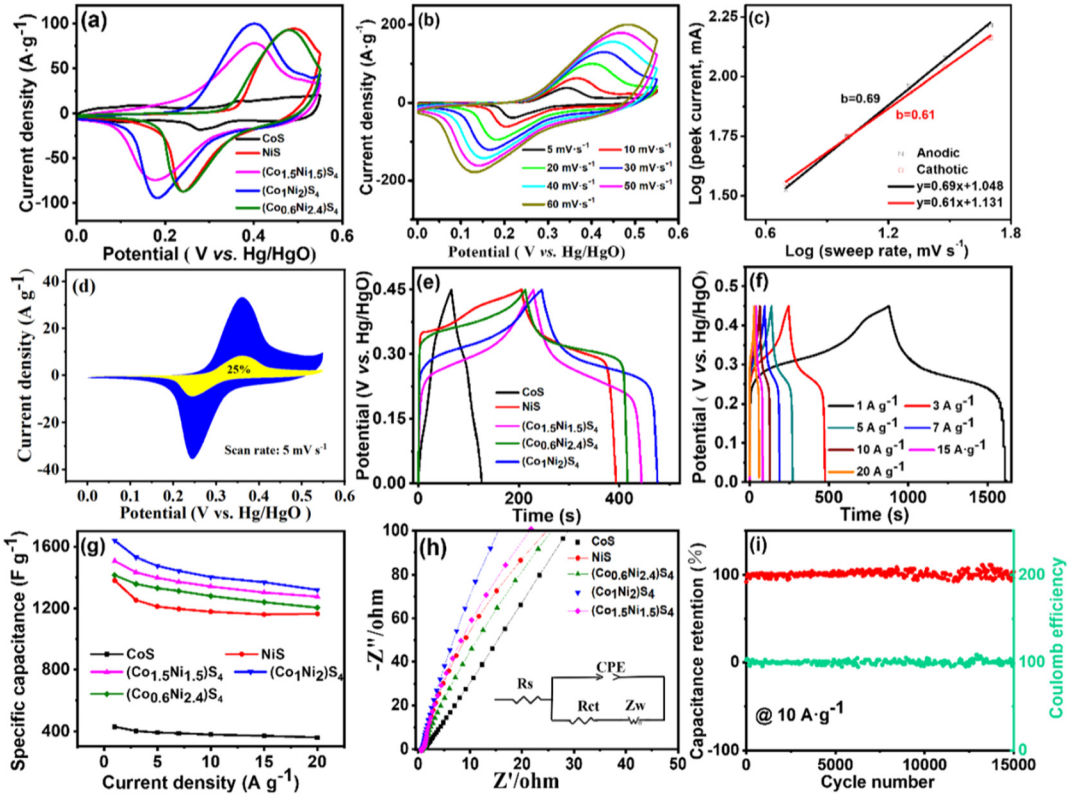

Fig. 4 (a) CV curves of the $Co_xNi_{3-x}S_4$ electrodes at a scan rate of 20 mV s^{-1}, (b) CV curves of the $(Co_1Ni_2)S_4$ electrode at different scan rates from 5 to 60 mV s^{-1}, (c) the linear relationship between the oxidation/reduction peak current density and scan rate of the $(Co_1Ni_2)S_4$ electrode, (d) separation of the diffusion and capacitive currents of the $(Co_1Ni_2)S_4$ electrode at 5 mV s^{-1}, (e) GCD curves of the $Co_xNi_{3-x}S_4$ electrodes at 3 A g^{-1}, (f) GCD curves of the $(Co_1Ni_2)S_4$ electrode at different current densities from 1 to 20 A g^{-1}, (g) capacitance retentions at different current densities and (h) Nyquist plots for $Co_xNi_{3-x}S_4$ electrodes, and (i) cycling stability at 10 A g^{-1}.

capacitive contribution steadily increases, achieving 52% at 50 mV s^{-1} (Fig. S10†). This indicates that surface capacitive charge storage plays a more significant role as scan rates become higher. Fig. 4e shows the GCD curves for CoS, NiS, $(Co_{1.5}Ni_{1.5})S_4$, $(Co_1Ni_2)S_4$ and $(Co_{0.6}Ni_{2.4})S_4$ at 3 A g^{-1}. Every electrode's GCD curve features a clear voltage plateau between 0.20 and 0.40 V and displays symmetrical curves, indicating high coulombic efficiency. The notably prolonged discharge period of $(Co_1Ni_2)S_4$, compared to those of other materials, emphasizes its outstanding energy storage potential, which matches the data obtained from CV analyses. To assess the efficiency and rate performance of the $(Co_1Ni_2)S_4$ electrode, GCD curves were measured at multiple current densities, varying from 1 A g^{-1} to 20 A g^{-1} (Fig. 4f). These curves display negligible potential drops across all tested current densities, highlighting the electrode's excellent conductivity and effective electrochemical interaction with electrolyte ions. Fig. 4g reveals that the highest specific capacity derived from the GCD curves is 204.9 mA h g^{-1} (1639 F g^{-1}) at 1 A g^{-1}, with a capacity of 165.0 mA h g^{-1} (1320 F g^{-1}) maintained at 20 A g^{-1}, achieving excellent rate capability.

In Fig. 4h, the EIS results are displayed, and the relevant parameters are listed in Table S2.† The EIS curve for the $(Co_1Ni_2)S_4$ electrode exhibited the smallest *x*-axis intercept and minimal semicircles, signifying the lowest internal resistance (R_s) of 0.61 Ω and a notably low charge transfer resistance (R_{ct}) of 0.27 Ω. In the low-frequency zone, the almost vertical line represents the Warburg impedance (W), and the $(Co_1Ni_2)S_4$ electrode displayed a sharper incline, signifying lower diffusion resistance. These observations confirm the high conductivity and electrochemical efficiency of the $(Co_1Ni_2)S_4$ electrode. Moreover, the cycling endurance of the $(Co_1Ni_2)S_4$ electrode was examined at 10 A g^{-1}, as depicted in Fig. 4i. After enduring 15 000 cycles, it retained 96% of its initial capacity, showcasing remarkable cycling stability.

For evaluating the practical applicability of the $(Co_1Ni_2)S_4$ electrode, an ASC was constructed with a 6 M KOH electrolyte. The negative electrode consisted of AC extracted from lotus pollen. As shown in Fig. 5a, the CV curves of both AC and $(Co_1Ni_2)S_4$ in a three-electrode configuration at a scan rate of 20 mV s^{-1} reveal that the AC electrode operates within a voltage window of −1 to 0 V and the $(Co_1Ni_2)S_4$ electrode within 0 to 0.55 V. Thus, it is evident that the ASC can achieve a maximum voltage window of 1.55 V. The CV curves, evaluated across different voltage ranges up to 1.65 V, as seen in

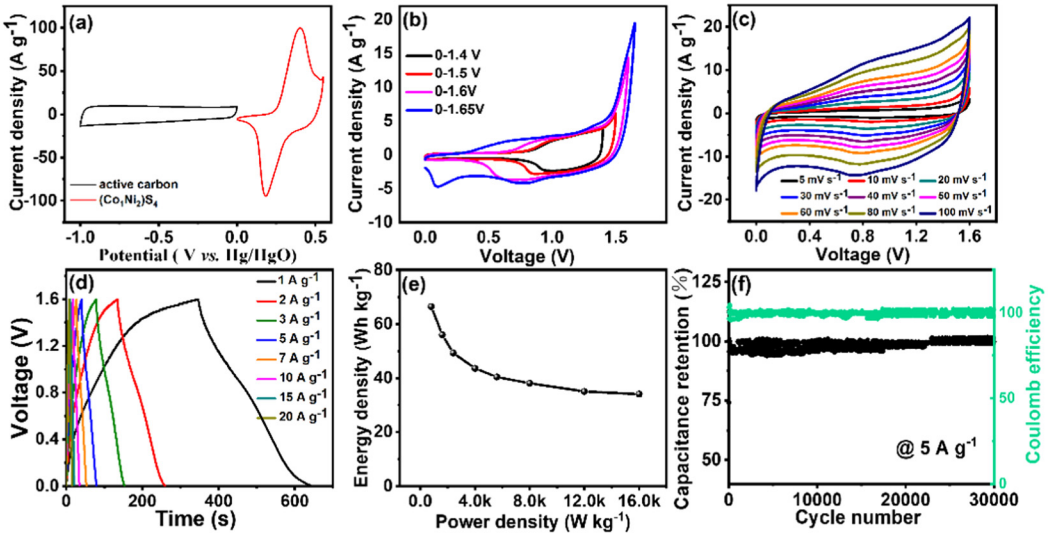

Fig. 5 Electrochemical capacitive performance of the $(Co_1Ni_2)S_4$//AC device: (a) CV curves of $(Co_1Ni_2)S_4$ and the AC electrode at 20 mV s^{-1} in a three electrode system, (b) CV curves of the ASC device in different voltage windows from 1.4 to 1.65 V, (c) CV curves of the ASC device at different scan rates from 5 to 100 mV s^{-1}, (d) GCD curves at different current densities, (e) gravimetric Ragone plot, and (f) cycling performance at 5 A g^{-1} for 30 000 cycles.

Table 1 Performance advantages of the $(Co_1Ni_2)S_4$//AC device with recently reported ASC devices[44–50]

ACS device	Energy density (W h kg^{-1})	Power density (W kg^{-1})	Capacity retention/cycles	Ref.
NiCoP@NiS//AC	30.47	800.07	82.22%/8000	44
Ni_7S_6@$NiCo_2S_4$//AC	53	810	87%/5000	45
r-$NiCo_2S_4$-6 HSs//N/S–AC	50.76	800	91.3%/5000	46
Co–MOF/NCS//AC	38.31	3175.3	88.07%/10 000	47
MoNiCoS@NF//AC/rGO	146.8	482.2	97%/5000	48
NiCo–DHS-12//HPAC	65.91	890	86.49%/8000	34
NCS–B3//CS	65	850	91.8%/8000	49
MWCNT–COOH@$NiCo_2S_4$//AC	33.6	375	83%/2000	50
$(Co_1Ni_2)S_4$//AC	66.5	800	98%/30 000	This work

AC: activated carbon; HPAC: hierarchically porous activated carbon; CS: carbon sphere; and NF: nickel foam.

Fig. 5b, were used to accurately identify the operational voltage window for the ASC. It becomes apparent that increased voltage ranges lead to more pronounced polarization, indicating an optimal voltage window of 1.6 V for the ASC. CV and GCD tests were performed at varying scan rates and current densities within this optimized 0 to 1.6 V range. All CV curves (Fig. 5c) show a semi-rectangular shape, indicating the effective combination of charge storage mechanisms in the AC and $(Co_1Ni_2)S_4$ electrodes. Additionally, the GCD curves of the $(Co_1Ni_2)S_4$//AC device exhibit good symmetry, confirming its good reversibility at 1.6 V, as seen in Fig. 5d. According to Fig. 5e, the $(Co_1Ni_2)S_4$//AC device achieves a maximum energy density of 66.5 W h kg^{-1} with a power density of 800 W kg^{-1}. Additionally, it provides an energy density of 34 W h kg^{-1} at 16 000 W kg^{-1}. Table 1 reveals that the $(Co_1Ni_2)S_4$-based ASC surpasses other recent cobalt–nickel sulfide-based asymmetric supercapacitors in energy storage performance, highlighting its suitability for practical energy storage solutions. The electrochemical properties of the ASC were examined *via* EIS, as illustrated in Fig. S12.† In the high-frequency segment of the plot, the extracted values for R_s and R_{ct} were 1.38 Ω and 0.35 Ω, respectively. Such low resistance values imply that electron transfer and ion transport within the device are highly efficient. After 30 000 cycles at 5 A g^{-1}, the ASC maintains 98% of its initial capacity along with 100% coulombic efficiency, reflecting its exceptional durability and stability (Fig. 5f). SEM images, after 30 000 cycles, reveal that despite a rougher surface, the hollow spherical structure of $(Co_1Ni_2)S_4$ is largely maintained (Fig. S13†). *Ex situ* XRD analysis shows that the diffraction peaks correspond to Co_3S_4 and Ni_3S_4. These results highlight the remarkable structural stability of $(Co_1Ni_2)S_4$ electrode materials, indicating their excellent potential for supercapacitor applications. These remarkable electrochemical properties are attributed to the combined benefits of a hierarchical porous hollow microsphere architecture and the synergistic interaction between cobalt and nickel sulfides.

4. Conclusion

We discovered that the electrochemical performance and morphology of cobalt–nickel bimetallic sulfides are greatly affected by the molar ratio between cobalt and nickel. By adjusting the synthesis process, we obtained cobalt–nickel bimetallic sulfides with hollow microsphere structures assembled from interwoven thin nanosheets, with nanoparticles uniformly dispersed on the surface of these nanosheets. This unique hierarchical structure combines the advantages of one-dimensional, two-dimensional, and three-dimensional architectures, facilitating the exposure of active sites, enhancing electron/ion transport, and alleviating volume expansion issues. Specifically, the $(Co_1Ni_2)S_4$ electrode material exhibited a specific capacity of 204.9 mA h g^{-1} (1639 F g^{-1}) at 1 A g^{-1}. Even at 20 A g^{-1}, it maintained a specific capacity of 165.0 mA h g^{-1}. After 15 000 cycles, the electrode retained 96% of its initial capacity. When paired with AC in an ASC, the $(Co_1Ni_2)S_4$//AC device achieved an energy density of 66.5 W h kg^{-1} at 800 W kg^{-1}. Impressively, after 30 000 cycles, the ASC still demonstrated an outstanding 98% capacitance retention. This study provides a promising strategy for the controlled synthesis of advanced bimetallic sulfides with enhanced electrochemical properties, laying the groundwork for their broader implementation in energy storage applications.

Data availability

The authors declare that data can be provided upon request.

Conflicts of interest

There are no conflicts to declare.

Acknowledgements

Financial support from the Outstanding Youth Fund of the Natural Science Foundation of Hubei Province (No. 2024AFA086) is gratefully acknowledged. We also extend our appreciation to Shiyanjia Lab (**https://www.shiyanjia.com**) for its support in materials characterization.

References

1 K. Dissanayake and D. Kularatna-Abeywardana, A review of supercapacitors: Materials, technology, challenges, and renewable energy applications, *J. Energy Storage*, 2024, **96**, 112563.
2 H. A. Behabtu, M. Messagie, T. Coosemans, M. Berecibar, K. A. Fante, A. A. Kebede and J. V. Mierlo, A review of energy storage technologies' application potentials in renewable energy sources grid integration, *Sustainability*, 2020, **12**, 10511.
3 L. L. Lyu, W. H. Antink, Y. S. Kim, C. W. Kim, T. Hyeon and Y. Z. Piao, Recent development of flexible and stretchable supercapacitors using transition metal compounds as electrode materials, *Small*, 2021, **17**, 2101974.
4 H. Su, C. Niu, R. Zhang, M. Huang and Z. Li, Construction of a $Ni_2P/NiSe_2/MoSe_2$ hybrid for advanced supercapacitors, *J. Alloys Compd.*, 2025, **1010**, 178074.
5 X. Mao, Y. J. Zou, F. Xu, L. Sun, H. Chu, H. Zhang, J. Zhang and C. Xiang, Three-dimensional hierarchical porous structures of metallic glass/copper composite catalysts by 3D printing for efficient wastewater treatments, *ACS Appl. Mater. Interfaces*, 2021, **13**, 22664.
6 S. Wang, Y. J. Zou, F. Xu, C. Xiang, H. Peng, J. Zhang and L. Sun, Morphological control and electrochemical performance of $NiCo_2O_4$@NiCo layered double hydroxide as an electrode for supercapacitors, *J. Energy Storage*, 2021, **41**, 102862.
7 Z. Li, J. Yu, C. Shi, H. Su and L. Bai, Controllable synthesis of porous $NiSe_2$ nanowires to boost energy storage performance for supercapacitors, *J. Energy Storage*, 2024, **91**, 112082.
8 L. Sun, K. L. Zhuo, Y. J. Chen, Q. Z. Du, S. J. Zhang and J. J. Wang, Ionic liquid-based redox active electrolytes for supercapacitors, *Adv. Funct. Mater.*, 2022, **32**, 2203611.
9 R. Liu, A. Zhou, X. Zhang, J. Mu, H. Che, Y. Wang, T. T. Wang, Z. Zhang and Z. Kou, Fundamentals, advances and challenges of transition metal compounds-based supercapacitors, *Chem. Eng. J.*, 2021, **412**, 128611.
10 M. Hashemi, M. S. Rahmanifar, M. F. El-Kady, A. Noori, M. F. Mousavi and R. B. Kaner, The use of an electrocatalytic redox electrolyte for pushing the energy density boundary of a flexible polyaniline electrode to a new limit, *Nano Energy*, 2018, **44**, 489.
11 S. Kula, K. R. Shrestha, G. Rajeshkhanna, N. H. Kim and J. H. Lee, Kirkendall growth and Ostwald ripening induced hierarchical morphology of Ni-Co LDH/$MMoS_x$ (M = Co, Ni, and Zn) heteronanostructures as advanced electrode materials for asymmetric solid-state supercapacitors, *ACS Appl. Mater. Interfaces*, 2019, **11**, 11555.
12 T. S. Le, T. K. Truon, V. N. Huynh, J. Bae and D. Suh, Synergetic design of enlarged surface area and pseudocapacitance for fiber-shaped supercapacitor yarn, *Nano Energy*, 2020, **67**, 104198.
13 X. Gao, X. Liu, D. Wu, B. Qian, Z. Kou, Z. Pan, Y. Pang, L. Miao and J. Wang, Significant role of Al in ternary layered double hydroxides for enhancing electrochemical performance of flexible asymmetric supercapacitor, *Adv. Funct. Mater.*, 2019, **5**, 1903879.
14 A. Agarwal and B. R. Sankapal, Metal phosphides: topical advances in the design of supercapacitors, *J. Mater. Chem. A*, 2021, **9**, 20241.
15 R. S. Redekar, S. S. Patil, P. S. Patil and N. L. Tarwal, Manganese cobalt oxide-polythiophene composite for asymmetric supercapacitor, *Chem. Eng. J.*, 2025, **503**, 158209.
16 P. Sharma and V. Kumar, Current technology of supercapacitors: A review, *J. Electron. Mater.*, 2020, **49**, 3520.

17 X. Zhu and S. Liu, Tremella-like 2D nickel-copper disulfide with ultrahigh capacity and cyclic retention for hybrid supercapacitors, *ACS Appl. Mater. Interfaces*, 2022, **14**, 43265.
18 Q. Hu, X. Zou, Y. Huang, Y. Wei, F. Chen, B. Xiang, Q. Wu and W. Li, Graphene oxide-drove transformation of NiS/Ni_3S_4 microbars towards Ni_3S_4 polyhedrons for supercapacitor, *J. Colloid Interface Sci.*, 2020, **559**, 115.
19 Y. Miao, X. Zhang, J. Zhan, Y. Sui, J. Qi, F. Wei, Q. Meng, Y. He, Y. Ren, Z. Zhan and Z. Sun, Hierarchical NiS@CoS with controllable core-shell structure by two-step strategy for supercapacitor electrodes, *Adv. Mater. Interfaces*, 2020, **7**, 1901618.
20 A. Mahieddine, L. Adnane-Amara, T. Tebaa and C. Saba, Core-shell structured hierarchical Ni nanowires and NiS/Co_3S_4 microflowers arrays as a high-performance supercapacitor electrode, *J. Energy Storage*, 2023, **57**, 106173.
21 D. Muhammad, X. Liu, H. Hou, X. Yu, J. Rong and J. Riaz, Noval synthesis of systematized FeS/CuO nanostructure efficacious electrode material for escalating asymmetric supercapacitors, *J. Alloys Compd.*, 2025, 178877.
22 A. M. Zardkhoshoui, B. Ameri and S. S. H. Davarani, α-MnS@Co_3S_4 hollow nanospheres assembled from nanosheets for hybrid supercapacitors, *Chem. Eng. J.*, 2021, **422**, 129953.
23 M. Huang, J. Yu, H. Su, Z. Wu and Z. Li, Coupling $(Ni_xCo_{1-x})_{0.85}Se$ with N-doped $MoSe_2$ for hybrid supercapacitors with remarkable cyclic durability, *Appl. Surf. Sci.*, 2025, **681**, 161547.
24 Z. Yu, S. Wang, Y. Huang, Y. J. Zou, F. Xu, C. Xiang, J. Zhang, J. Xie and L. Sun, Bi_2O_3 nanosheet-coated $NiCo_2O_4$ nanoneedle arrays for high-performance supercapacitor electrodes, *J. Energy Storage*, 2022, **55**, 105486.
25 X. Yang, C. Xiang, Y. Zou, J. Liang, H. Zhang, E. Yan, F. Xu, X. Hu, Q. Cheng and L. Sun, Low-temperature synthesis of sea urchin-like Co-Ni oxide on graphene oxide for supercapacitor electrodes, *J. Mater. Sci. Technol.*, 2020, **55**, 223.
26 Z. Li, Y. Qu, M. Wang, Y. Hu, J. Han, L. Fan and R. Guo, O/W interface-assisted hydrothermal synthesis of $NiCo_2S_4$ hollow spheres for high-performance supercapacitors, *Colloid Polym. Sci.*, 2016, **294**, 1325.
27 Q. Li, M. Liu, F. Huang, X. Zuo, X. Wei, S. Li and H. Zhang, Co_9S_8@MnO_2 core-shell defective heterostructure for high-voltage flexible supercapacitor and Zn-ion hybrid supercapacitor, *Chem. Eng. J.*, 2022, **437**, 135494.
28 G. Wu, Z. Ma, X. Wu, X. Zhu, Z. Man, W. Lu and J. Xu, Interfacial polymetallic oxides and hierarchical porous core-shell fibres for high energy-density electrochemical supercapacitors, *Angew. Chem., Int. Ed.*, 2022, **61**, e202203765.
29 A. I. Abdel-Salam, S. Y. Attia, S. G. Mohamed, F. I. El-Hosiny, M. A. Sadek and M. M. Rashad, Designing a hierarchical structure of nickel-cobalt-sulfide decorated on electrospun N-doped carbon nanofiber as an efficient electrode material for hybrid supercapacitors, *Int. J. Hydrogen Energy*, 2023, **48**, 5463.
30 N. Septiani, S. Chowdhury, A. Hardiansyah, M. Rinawati, M. Yeh, H. Nara, Y. Yamauchi, Y. V. Kaneti and B. Yuliarto, Selective synthesis of monodisperse bimetallic nickel-cobalt phosphates with different nanoarchitectures for battery-like supercapacitors, *J. Mater. Chem. A*, 2024, **12**, 14045.
31 Z. Li, X. Ji, J. Han, Y. Hu and R. Guo, $NiCo_2S_4$ nanoparticles anchored on reduced graphene oxide sheets: *in situ* synthesis and enhanced capacitive performance, *J. Colloid Interface Sci.*, 2016, **477**, 46.
32 C. Kang, L. Ma, Y. Chen, L. Fu, Q. Hu, C. Zhou and Q. Liu, Metal-organic framework derived hollow rod-like NiCoMn ternary metal sulfide for high-performance asymmetric supercapacitors, *Chem. Eng. J.*, 2022, **427**, 131003.
33 J. Qi, H. Duan, Z. Peng, J. Wang, B. Ma, Z. Yuan and H. Zhang, Cobalt-nickel mixed metal sulfide hollow nanocages with enhanced surface-induced capacitive storage for hybrid supercapacitor, *Energy Fuels*, 2024, **38**, 13379.
34 S. Jia, Y. Y. Lv, J. Wei, J. Guan, Y. Zhai and Z. Q. Shao, Amorphous nanosheets constructed nickel cobalt hydroxysulfide hollow spheres as cathode materials for hybrid supercapacitors, *Chem. Eng. J.*, 2023, **456**, 141120.
35 X. K. Xiong, J. Jin, M. Xie, J. Chen, Y. Zhang, L. Wan and C. Du, Cobalt-nickel sulfide hierarchical hollow microspheres to boost electrochemical activity for supercapacitors, *J. Alloys Compd.*, 2025, **1010**, 177730.
36 Y. Ma, H. Wang, W. Lv, S. Ji, B. Pollet, S. Li and R. Wang, Amorphous PtNiP particle networks of different particle sizes for the electro-oxidation of hydrazine, *RSC Adv.*, 2015, **5**, 68655.
37 S. Bhattacharyya, A. Gabashvili, N. Perkas and A. Gedanken, Sonochemical insertion of silver nanoparticles into two-dimensional mesoporous alumina, *J. Phys. Chem. C*, 2007, **111**, 11161.
38 F. Ning, M. Shao, C. Zhang, S. Xu, M. Wei and X. Duan, Co_3O_4@layered double hydroxide core/shell hierarchical nanowire arrays for enhanced supercapacitance performance, *Nano Energy*, 2014, **7**, 134.
39 X. Ling, W. Wei, C. Shan, X. Qin, M. Song, Z. Liu and L. Mi, Ball-in-ball NiS_2@CoS_2 heterojunction driven by Kirkendall effect for high-performance Mg^{2+}/Li^+ hybrid batteries, *J. Colloid Interface Sci.*, 2024, **658**, 688.
40 Y. Su, X. Liu, R. Zhang, S. Zhang, J. Wang, Y. Qian, Z. Jian, Y. Zhu, J. Mao, S. Xu, S. Dou and Y. Xiao, A dual-confinement strategy based on encapsulated Ni-CoS_2 in CNTs with few-layer MoS_2 scaffolded in rGO for boosting sodium storage via rapid electron/ion transports, *Energy Storage Mater.*, 2024, 103638.
41 D. Zhao, M. Dai, H. Liu, K. Chen, X. Zhu, D. Xue, X. Wu and J. Liu, Sulfur–induced interface engineering of hybrid $NiCo_2O_4$@$NiMo_2S_4$ structure for overall water splitting and flexible hybrid energy storage, *Adv. Mater. Interfaces*, 2019, **6**, 1901308.
42 C. Xia, P. Li, A. N. Gandi, U. Schwingenschlögl and H. N. Alshareef, Is $NiCo_2S_4$ really a semiconductor?, *Chem. Mater.*, 2015, **27**, 6482.

43 D. Jiang, Y. Wang, C. Du, M. Xie, J. Chen, Y. Zhang and L. Wan, Heterostructured Ni_2P/NiMo-layered double hydroxide nanoarrays with enriched redox active sites for supercapacitors, *J. Alloys Compd.*, 2024, **970**, 172685.
44 Y. X. Dong, X. Q. Yue, Y. Liu, Q. J. Zheng, Z. Q. Cao and D. M. Lin, Hierarchical core-shell-structured bimetallic nickel-cobalt phosphide nanoarrays coated with nickel sulfide for high-performance hybrid supercapacitors, *J. Colloid Interface Sci.*, 2022, **628**, 222.
45 Q. L. Sui, J. Li, C. L. Xiang, F. Xu, J. Zhang, L. X. Sun and Y. J. Zou, Nickel metal-organic framework microspheres loaded with nickel-cobalt sulfides for supercapacitor electrode materials, *J. Energy Storage*, 2022, **55**, 105525.
46 S. Jia, J. Wei, B. X. Gong, J. Wei and Z. Q. Shao, Sulfur vacancies enriched nickel-cobalt sulfides hollow spheres with high performance for all-solid-state hybrid supercapacitor, *J. Colloid Interface Sci.*, 2021, **601**, 640.
47 N. B. Velhal, N. C. Maile, C. G. Paeng, H. J. Lee, T. Kim, J. Kim and C. Y. Yim, Cobalt-based metal-organic framework/nickel-cobalt sulphide composite nanopetal arrays for high-performance hybrid coin cell supercapacitor, *J. Energy Storage*, 2024, **90**, 111764.
48 U. Evariste, G. H. Jiang, B. Yu, Y. K. Liu and P. P. Ma, One-step electrodeposition of molybdenum nickel cobalt sulfides on Ni foam for high-performance asymmetric supercapacitors, *J. Energy Storage*, 2020, **29**, 101419.
49 J. X. Gong, Y. R. Wang, J. H. Wang, Y. X. Liu, C. H. Hu, T. L. Zhou, Q. L. Yu, J. X. Yang and Y. T. Dai, Hollow nickel-cobalt sulfide nanospheres cathode hybridized with carbon spheres anode for ultrahigh energy density asymmetric supercapacitors, *Int. J. Hydrogen Energy*, 2022, **47**, 10056–10068.
50 Z. Li, Y. Xin, H. Jia, J. Sun and Q. Zhou, Rational design of coaxial MWCNT-COOH@$NiCo_2S_4$ hybrid for supercapacitors, *J. Mater. Sci.*, 2017, **52**, 9661.